

Citation for published version:

Puzyrev, D & Skryabin, D 2021, 'Finesse and four-wave mixing in microresonators', *Physical Review A*, vol. 103, no. 1, 013508. <https://doi.org/10.1103/PhysRevA.103.013508>

DOI:

[10.1103/PhysRevA.103.013508](https://doi.org/10.1103/PhysRevA.103.013508)

Publication date:

2021

Document Version

Peer reviewed version

[Link to publication](#)

(C) 2021 American Physical Society

University of Bath

Alternative formats

If you require this document in an alternative format, please contact:
openaccess@bath.ac.uk

General rights

Copyright and moral rights for the publications made accessible in the public portal are retained by the authors and/or other copyright owners and it is a condition of accessing publications that users recognise and abide by the legal requirements associated with these rights.

Take down policy

If you believe that this document breaches copyright please contact us providing details, and we will remove access to the work immediately and investigate your claim.

Finesse and four-wave mixing in microresonators

D.N. Puzyrev and D.V. Skryabin*

Department of Physics, University of Bath, Bath BA2 7AY, UK

We elaborate a comprehensive theory of the sharp variations of the four-wave-mixing (FWM) threshold happening with the tuning of the pump frequency along the dispersive tails of the nonlinear resonance in the driven Kerr microresonators with high finesse and high finesse dispersions. Our theory leads to the explicit estimates for the difference in the pump powers required for the excitation of one sideband pair with momenta $\pm\mu$, and for the simultaneous excitation of the two neighbouring pairs with momenta $\pm\mu, \pm(\mu+1)$. This power difference also measures the depth of the Arnold tongues in the pump-frequency and pump-power parameter space, associated with the aforementioned power variations. A set of select pump frequencies and powers, where the instabilities of the two sideband pairs come first, forms the threshold of complexity, which is followed by a sequence of conditions specifying critical powers for the simultaneous instabilities of three, four and so on pairs. We formally link finesse dispersion and the density of states notion borrowed from the condensed matter context, and report a value of the finesse dispersion and a critical mode number signalling the transition from the low- to the high-contrast tongue structure. We also demonstrate that the large finesse dispersion makes possible a surprising for the multimode resonators regime of the bistability without FWM.

I. INTRODUCTION

Maxwell and Schroedinger equations are the fundamental laws of nature governing interaction of photons and electrons. Optically pumped resonators boost the number of incoming photons interacting with the intra-resonator matter by a factor determined by the inter-mode frequency separation divided by the linewidth, i.e., finesse. Thereby, the high-finesse resonators are the devices enabling modern research into strong light-matter interaction [1] and frequency conversion [2]. In this work, we present a comprehensive analytical theory for the four-wave mixing (FWM) threshold in the high-finesse Kerr resonators. Our research is underpinned by the relentless push towards achieving ever-high quality factors in the bulk and chip-integrated microresonators, see, e.g., [3–7].

Since the very early days of theoretical research into nonlinear physics of optical resonators, it has been acknowledged that the Maxwell and Schroedinger equations can be reduced to either a system of coupled ordinary differential equations (ode's) for the time evolution of mode amplitudes [8] or a system of partial differential equations (pde's) for the envelope functions [9]. Two approaches are in fact equivalent providing a pde is supplemented by the boundary conditions that admit the mode profiles used to derive the ode's [9, 10]. A high-quality ring microresonator [2, 11] is an example where the aforementioned equivalence is particularly vivid, since the azimuthally rotating modes, $e^{i\mu\vartheta - i\omega_\mu t}$, constitute a quasi-exact basis for nonlinear Maxwell equations and the exact one for their reduction to the Lugiato-Lefever equation (LLE) conditioned by the 2π -periodicity in ϑ [12–16], see, e.g., Refs. [17] for general and Ref. [18] for the derivation focused overviews.

Thus, either the pde or ode formulations allow investigating the impact of the finesse on FWM and other types of frequency conversion in microresonators. Recently, we have contributed to the microresonator theory by demonstrating that the threshold condition for the degenerate FWM in the high-finesse devices breaks the pump laser parameter space into a sequence of narrow in frequency and broad in power Arnold tongues [19]. Large finesse \mathcal{F} is normally accompanied by the relatively large finesse dispersion, \mathcal{F}_d , which is a key parameter behind the tongue formation. Instability tongues become a dominant feature in resonators with \mathcal{F}_d approaching unity and disappear if \mathcal{F}_d is relatively small. The latter case recovers the multimode threshold shapes reported in Refs. [16, 20]. Ref. [20] followed a series of pioneering experiments on FWM in microresonators [21–23] and the three-mode, i.e., pump-signal-idler, theory of the microresonator FWM [24].

Ref. [19] has addressed few interesting problems with the FWM emerging in the ultrahigh- \mathcal{F} devices. First, is that looking at the superposition of the individual thresholds for generation of the $\pm\mu$ sideband pairs, one can observe dramatic reshaping of the net threshold when the finesse dispersion, \mathcal{F}_d , is increased. Second, is that the intersections of the instabilities domains corresponding to $\pm\mu$ and $\pm(\mu+1)$ modes touch the stability intervals of the single-mode state and therefore constitute a threshold condition - *threshold of complexity*. These effects are happening along the dispersive tails of the nonlinear resonance for positive detunings if dispersion is normal, $\mathcal{F}_d < 0$, and for the negative detunings if dispersion is anomalous, $\mathcal{F}_d > 0$. Elegant mathematics and important physics behind deriving the power and detuning values corresponding to the threshold of complexity could not be given the attention they deserve in the short format of Ref. [19] and their detailed description is presented to the readers below. We also cover here a range of connected problems not directly addressed by Ref. [19].

* d.v.skryabin@bath.ac.uk

This work is organised in several sections and multiple subsections:

Section II introduces a model (II.A), notations and parameters, including the residual finesse, $\alpha_\mu = (\mu + \frac{1}{2})\mathcal{F}_d$, which is the key parameter in our study (II.B). (II.C) introduces transparent power scaling allowing an immediate link to physical quantities of interest. (II.D) covers in details the classic results [25] on the cw-state stability using relevant for us notations and terminology. It sets the scene for revealing the role of the interplay between the different $|\mu|$ in the cw-stability analysis, which constitutes the main content of the following sections.

Section III provides comprehensive description of the visualised numerical data on the interplay between the instabilities for different $|\mu|$, and of the threshold reshaping for the residual spectrum changing from the quasi-continuous to sparse. It takes an advantage of using the side-band coupling constant, g , for these purposes, and discusses details of nonlinear mapping between g , which is proportional to the intra-resonator power, and the pump laser power.

Section IV is central. It solves conditions on g , along the threshold of complexity (IV.A, IV.B). It then works out critical values for $\mu = \hat{\mu}$, $\alpha_\mu = \alpha_{\hat{\mu}}$, and for the laser detuning that can be used to characterise transition to the Arnold-tongue regime (IV.C). IV.D derives the $|\mathcal{F}_d| > 2/\sqrt{3}$ condition for the Arnold tongues to dominate for all detunings, and demonstrates an unusual for the multimode resonators regime of the bistability without FWM.

Section V presents comprehensive explicit analytical results for the sideband coupling constant and laser power along the threshold of complexity. It provides an overarching diagram characterising occurrences of the different FWM instabilities in the high-finesse resonators.

Section VI provides further contextual links. Section VII summarizes the results.

II. BACKGROUND

A. Microresonator LLE (mLLE)

The mLLE model is [17, 18]

$$\begin{aligned} i\partial_t\psi &= \delta_0\psi - \frac{1}{2}D_2\partial_\theta^2\psi - i\frac{1}{2}\kappa(\psi - \mathcal{H}) - \gamma|\psi|^2\psi, \quad (1a) \\ \theta &= \vartheta - D_1t, \quad (1b) \end{aligned}$$

where $\delta_0 = \omega_0 - \omega_p$ is detuning of the pump laser frequency, ω_p , from the ω_0 resonance. ϑ is the angular coordinate in the laboratory reference frame. $D_1/2\pi > 0$ is the non-dispersive part of the resonator repetition rate, which equals the nondispersive part of the FSR. D_2 is the 2nd order dispersion. κ is the linewidth. \mathcal{H}^2 is the intra-resonator pump power. γ is the nonlinear parameter [18],

$$\gamma = \frac{\omega_0 n_2}{2S n_0}, \quad (2)$$

where n_2 is Kerr coefficient, n_0 is refractive index, and S is the transverse mode area.

Transformation to the rotating reference frame, $\vartheta \rightarrow \theta$, and counting resonances from ω_0 replaces the bare resonator spectrum

$$\begin{aligned} \omega_\mu &= \omega_0 + D_1\mu + \frac{1}{2}D_2\mu^2, \quad (3) \\ \mu &= -\frac{1}{2}N + 1, \dots, 0, \dots, \frac{1}{2}N, \end{aligned}$$

with the residual, i.e., linear mLLE, spectrum

$$\Delta_\mu = \delta_0 + \frac{1}{2}\mu^2 D_2. \quad (4)$$

Let us make a note, that all the theory is developed here in physical units. In particular, δ_0, κ, D_2 have units of Hz. $|\psi|^2, \mathcal{H}^2$ are measured in Watts, and γ is in Hz/Watt.

B. Finesse, residual finesse and density of states

Resonator finesse, \mathcal{F}_μ , is a relative to the linewidth and the mode-number specific measure of the resonance separation,

$$\frac{\omega_{\mu+1} - \omega_\mu}{\kappa} = \mathcal{F}_\mu = \frac{D_1}{\kappa} + \frac{D_2(\mu + \frac{1}{2})}{\kappa}, \quad \mu \geq 0, \quad (5a)$$

$$\frac{\omega_\mu - \omega_{\mu-1}}{\kappa} = \mathcal{F}_\mu = \frac{D_1}{\kappa} + \frac{D_2(\mu - \frac{1}{2})}{\kappa}, \quad \mu \leq 0. \quad (5b)$$

Here,

$$\mathcal{F} = \frac{D_1}{\kappa}, \quad \text{and} \quad \mathcal{F}_d = \frac{D_2}{\kappa} \quad (6)$$

are the dispersion free finesse and finesse dispersion, respectively.

Following Ref. [19], we define a rule to calculate frequencies in the residual spectrum,

$$\frac{\Delta_{\mu+1} - \Delta_\mu}{\kappa} = \alpha_\mu, \quad \alpha_\mu = \mathcal{F}_d(\mu + \frac{1}{2}), \quad \mu \geq 0, \quad (7a)$$

$$\frac{\Delta_\mu - \Delta_{\mu-1}}{\kappa} = \alpha_\mu, \quad \alpha_\mu = \mathcal{F}_d(\mu - \frac{1}{2}), \quad \mu \leq 0. \quad (7b)$$

Here, α_μ is the residual finesse defining the mode-number specific separation of the resonances in the residual spectrum [19]. Residual spectrum is non-equidistant and the resonance separation is increasing with $|\mu|$. \mathcal{F}_d is the prime and only parameter controlling this nonequidistance. $|\alpha_\mu| \ll 1$ corresponds to the quasi-continuous residual spectrum and $|\alpha_\mu| \gg 1$ to the sparse one. For microresonators, \mathcal{F} is typically the order of 10^3 to 10^6 , while $|\mathcal{F}_d|$ is the order of 10^{-3} to 10 , so that $\mathcal{F} \gg |\mathcal{F}_d|$.

Definition of the residual finesse directly connects to the density of optical states (DoS) concept [26, 27]. Taking the $\mathcal{L}_\mu = 2|\mu|$ length span in the momentum space, we apply the text-book definition of the density of states [28], \mathcal{D}_μ , to the κ -normalised residual spectrum,

$$\mathcal{D}_\mu = \frac{d\mathcal{L}_\mu}{d|\mu|} \cdot \left[\frac{d(\Delta_\mu/\kappa)}{d|\mu|} \right]^{-1} = \frac{2}{|\mu|\mathcal{F}_d} \approx \frac{2}{\alpha_{|\mu|}}. \quad (8)$$

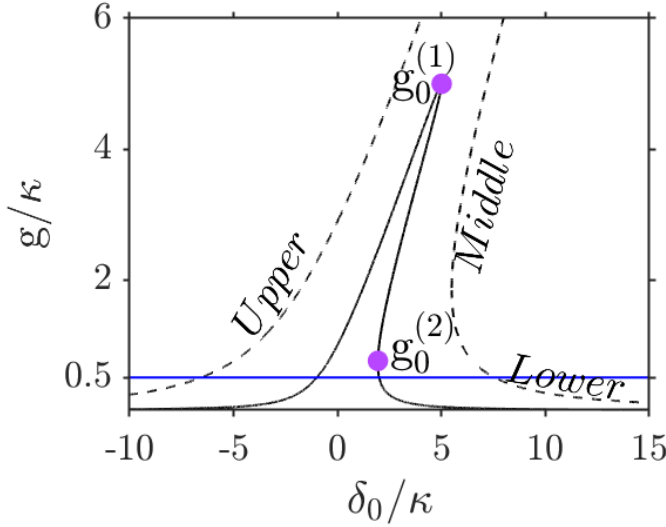


FIG. 1. Normalised intra-resonator cw-state power computed from Eq. (12): $W/W_* = 5$ (full line), $W/W_* = 100$ (dashed line). Horizontal blue line shows the FWM threshold as per Eq. (22b). Magenta points are given by Eqs. (16) for $\mu = 0$. g/γ equals the intra-resonator cw power in Watts, see Table I.

Thus DoS is inversely proportional to the residual finesse. If DoS is close to and less than 1, then the residual spectrum is sparse.

C. Power scaling

If the power coupling efficiency is $\eta = \kappa_c/\kappa < 1$, and κ_c is the coupling loss, then the laser power, \mathcal{W} , that couples to a ring resonator is calculated as [33]

$$\mathcal{W} = \frac{\pi}{\eta \mathcal{F}} \mathcal{H}^2. \quad (9)$$

We introduce here the characteristic power scales \mathcal{W}_* and κ/γ for the 'on-chip' laser power and for the intra-resonator power, respectively,

$$\mathcal{W}_* = \frac{\pi}{\eta} \frac{\kappa^2}{D_1 \gamma}, \quad \frac{\mathcal{W}}{\mathcal{W}_*} = \frac{\mathcal{H}^2}{\kappa/\gamma}. \quad (10)$$

We note, that D_1 is inversely proportional to the resonator length and $\gamma \sim 1/S$, hence $\mathcal{W}_* \sim V$, where V is the mode volume. Also, $\kappa = \omega_0/Q$, where Q is the quality factor. Hence, $\mathcal{W}_* \sim V/Q^2$, which is in the agreement with the laser power FWM threshold scaling previously used and derived in connection with the microresonator FWM [17, 21–24].

Appendix provides detailed estimates for the parameters, while Table I sums up the quality factors, linewidths, finesse dispersions, and power scaling factors for typical microresonator examples. All our results and data are given in the transparently scaled form, so that

TABLE I. Parameters for the bulk crystalline CaF_2 and integrated Si_3N_4 resonators, see Appendix and text for further details. Q is quality factor, κ is linewidth, $\mathcal{F}_d = D_2/\kappa$ is finesse dispersion, \mathcal{W}_* is the laser pump power scale, and κ/γ is the intra-resonator power scale.

Q	$\kappa/2\pi$	$ \mathcal{F}_d $	\mathcal{W}_*	κ/γ
CaF_2				
10^9	200 kHz	0.005	1 mW	20 W
10^{11}	2 kHz	0.5	0.1 μW	0.2 W
Si_3N_4				
10^6	100 MHz	0.5	4 mW	5 W
10^7	10 MHz	5	40 μW	0.5 W

a reader can either customise the scales if needed, or see directly how and if the numbers in Table I fit with the characteristics of the available or projected samples of their interest.

D. CW-state and its stability

We define the intra-resonator power of the single-mode cw-solution of Eq. (1) via the identity $|\psi|^2 = g/\gamma$, where the newly introduced parameter $g \geq 0$ has units of frequency. Then, the complex cw, i.e., continuous wave, amplitude is

$$\psi = \sqrt{\frac{g}{\gamma}} e^{i\phi_0} = \frac{-i\frac{1}{2}\kappa\mathcal{H}}{\delta_0 - g - i\frac{1}{2}\kappa}, \quad (11)$$

where $\phi_0 = \arg \psi_0$. Taking absolute value of Eq. (11) yields the bistability equation,

$$\frac{g}{\kappa} + \frac{4g}{\kappa} \left(\frac{\delta_0}{\kappa} - \frac{g}{\kappa} \right)^2 = \frac{\gamma \mathcal{H}^2}{\kappa} = \frac{\mathcal{W}}{\mathcal{W}_*}, \quad (12)$$

see Fig. 1. In order to estimate the intra-resonator cw power, g/γ , the dimensionless g/κ parameter shown in Fig. 1 and used through the rest of the text and figures should be multiplied by κ/γ , see Table I for some typical values.

Perturbing the cw with a pair of sideband modes [25],

$$\psi = \sqrt{g/\gamma} e^{i\phi_0} + \psi_\mu e^{i\mu\theta} + \psi_{-\mu}^* e^{-i\mu\theta}, \quad (13)$$

and setting $\psi_{\pm\mu} \sim e^{\lambda_\mu t}$ gives

$$i\lambda_\mu \begin{bmatrix} \psi_\mu \\ \psi_{-\mu} \end{bmatrix} = \begin{bmatrix} \Delta_\mu - 2g - i\frac{1}{2}\kappa & -ge^{i2\phi_0} \\ ge^{-i2\phi_0} & -\Delta_\mu + 2g - i\frac{1}{2}\kappa \end{bmatrix} \begin{bmatrix} \psi_\mu \\ \psi_{-\mu} \end{bmatrix}, \quad (14)$$

and hence

$$\begin{aligned} \lambda_\mu (\lambda_\mu + \kappa) &= 3(g_\mu^{(1)} - g)(g - g_\mu^{(2)}) \\ &= 3(\Delta_\mu - g)(g - \frac{1}{3}\Delta_\mu) - \frac{1}{4}\kappa^2, \end{aligned} \quad (15)$$

where

$$\frac{g_\mu^{(1)}}{\kappa} = \frac{2}{3} \frac{\Delta_\mu}{\kappa} + \frac{1}{3} \sqrt{\frac{\Delta_\mu^2}{\kappa^2} - \frac{3}{4}}, \quad (16a)$$

$$\frac{g_\mu^{(2)}}{\kappa} = \frac{2}{3} \frac{\Delta_\mu}{\kappa} - \frac{1}{3} \sqrt{\frac{\Delta_\mu^2}{\kappa^2} - \frac{3}{4}}. \quad (16b)$$

g couples the ψ_μ and $\psi_{-\mu}$ sidebands, cf., Refs. [19, 24]. The coupling is anti-Hermitian, and therefore it provides gain and seeds the instability.

Eq. (15) has two roots,

$$\lambda_\mu^\pm = -\frac{1}{2}\kappa \pm \sqrt{3(\Delta_\mu - g)(g - \frac{1}{3}\Delta_\mu)}. \quad (17)$$

The real part of λ_μ^- is unconditionally negative, while the other root yields the threshold condition, $\text{Re}\lambda_\mu^+ = \lambda_\mu^+ = 0$,

$$g = g_\mu^{(1)}, g = g_\mu^{(2)}, \quad (18)$$

with

$$g_\mu^{(2)} < g < g_\mu^{(1)} \quad (19)$$

being an interval of g with the exponential growth of the sideband powers. Thus, $g_\mu^{(i)} \geq 0$, $i = 1, 2$, are the critical values of the $\pm\mu$ sideband coupling limiting the respective FWM gain range from below, $i = 2$, and from above, $i = 1$. Eq. (19) can be compared with the cw instability interval reported in Ref. [25] and using $\frac{1}{2}\mu^2\mathcal{F}_d$ as a control parameter.

Two lines, $g = g_\mu^{(i)}$, merge at $g_\mu^{(1)} = g_\mu^{(2)}$, and extend for

$$\frac{\Delta_\mu}{\kappa} \geq \frac{\sqrt{3}}{2} \quad (20)$$

through the $|\mu|$ -instability range. The value of g corresponding to the equal sign in Eq. (20) is

$$\frac{g}{\kappa} = \frac{1}{\sqrt{3}} = \frac{g_\mu^{(1)}}{\kappa} = \frac{g_\mu^{(2)}}{\kappa}. \quad (21)$$

The minimum of $g_\mu^{(2)}$ in δ_0 corresponds to the lowest intra-resonator power, $g_\mu^{(2)}/\gamma$, required to kick-start FWM for a given $\pm\mu$ pair, i.e., to the *FWM threshold*. Coordinates of the minimum are

$$\frac{\Delta_\mu}{\kappa} = 1, \quad (22a)$$

$$\frac{g}{\kappa} = \frac{1}{2} = \min_{\delta_0} \frac{g_\mu^{(2)}}{\kappa}. \quad (22b)$$

For $\kappa = 2$, Eqs. (22) match equations for $a(n_c)$ and E_s from Ref. [25].

The $g_\mu^{(2)}$ values at their minima are μ independent, while recovering δ_0 at the same points from Eq. (22a) and Eq. (4) gives

$$\frac{\delta_0^{(\mu F)}}{\kappa} = 1 - \frac{1}{2}\mu^2\mathcal{F}_d. \quad (23)$$

Let us note, that stability analysis in this subsection did not touch on the problem of the interplay between the sidebands with different $|\mu|$, and therefore did not require using the residual finesse, α_μ . All this becomes central in what follows.

III. INSTABILITIES, TONGUES AND THRESHOLDS

Insight into the intersections, which presence or absence is also not immediately obvious, of the stability boundaries given by Eqs. (19) for different μ in the space of physical parameters reveals how a resonator transits from the stable cw-state to the sideband generation [19]. To investigate how the transition from the quasi-continuous, $|\alpha_\mu| \ll 1$, to sparse, $|\alpha_\mu| \gg 1$, residual spectra impacts the net instability threshold one can plot the threshold laser power, \mathcal{W} , vs δ_0 for every $\mu \in \mathbb{Z}$ and different \mathcal{F}_d , see Figs. 2, 3. The respective powers are calculated by substituting $g_\mu^{(i)}$ into Eq. (12) and using Eqs. (9), (10),

$$\frac{\mathcal{W}_\mu^{(i)}}{\mathcal{W}_*} = \frac{g_\mu^{(i)}}{\kappa} + \frac{4g_\mu^{(i)}}{\kappa} \left(\frac{\delta_0}{\kappa} - \frac{g_\mu^{(i)}}{\kappa} \right)^2, \quad (24)$$

Eq. (24) is dimensionless and parameterised by the finesse dispersion, \mathcal{F}_d , and, by the normalised laser detuning, δ_0/κ .

To facilitate with the theory developed below it is important to analyse the $g = g_\mu^{(i)}$ vs δ_0 plots, see Figs. 2-4. For $|\mathcal{F}_d| \ll 1$ the common envelope of the threshold lines flattens and approaches the $g/\kappa = 1/2$ line, see Fig. 2(a). Instead, with $|\mathcal{F}_d|$ increasing and approaching one, the instability tongues are shaping up with the gradually increasing power (vertical) contrast and frequency (horizontal) sparsity, see Fig. 3 and Ref. [19]. The Arnold-tongue structure implies that small changes of the pump frequency can lead to the large variations in the power threshold, cf., Figs. 2(b) and 3(b). The $|\mu| \neq 0$ tongues unfold either left or right from the $\mu = 0$ one, depending on the sign of \mathcal{F}_d , cf., Fig. 3(c) for normal dispersion and, e.g., Fig. 3(a) for anomalous.

In the nonlinear dynamics, Arnold tongues are classified by their synchronisation order $n : m$, where n is the number of nonlinear pulses coming through the system per m periods of the linear oscillator [29]. In our case, the linear round trip time is $2\pi/D_1$ and periods of the synchronised waveforms given Eqs. (13), (1b) are $2\pi/|\mu|D_1$, thus the corresponding orders are $|\mu| : 1$. Practically, mLLE Arnold tongues are defined as per the convergence of their minima to the points of resonances, $\Delta_\mu = 0$, in the linear residual spectrum, i.e., for $g, \kappa \rightarrow 0$, [19, 29]. Only the dispersive tails of the cw-resonance, see Fig. 1, withstand the $g \rightarrow 0$ limit. While $\Delta_\mu = 0$ opens up as $\delta_0 = -\frac{1}{2}\mu^2 D_2$, and hence the linear resonances occur for $D_2 > 0$ at $\delta_0 < 0$, i.e., along the tail of the upper branch,

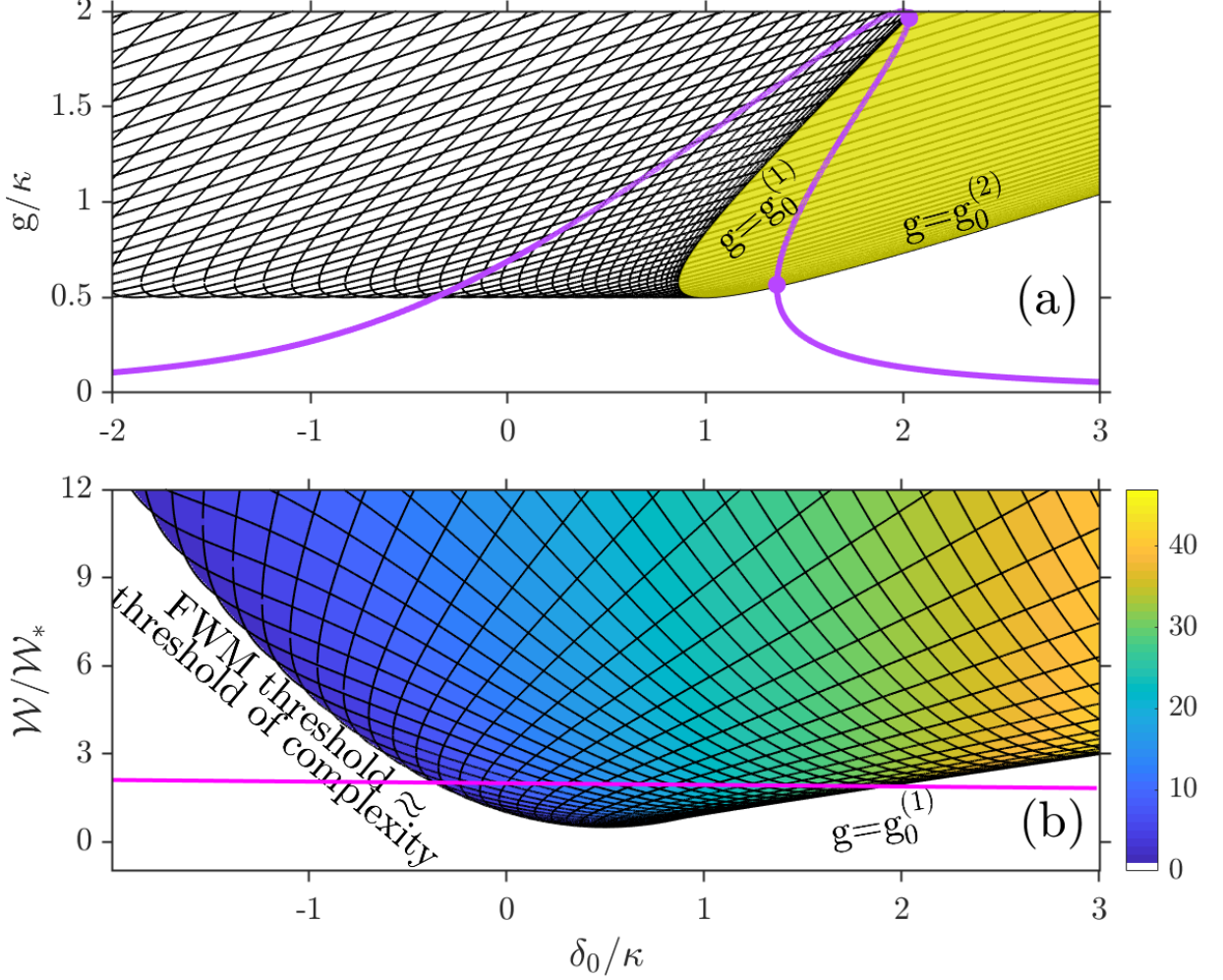


FIG. 2. An illustration of how the quasi-continuous residual spectrum, $|\mathcal{F}_d| = |D_2|/\kappa \ll 1$, leads to the coinciding FWM and complexity thresholds. **(a)** $g/\kappa = g_\mu^{(i)}/\kappa$ vs δ_0/κ for $\mu = 0, 1, \dots, 64$ and $\mathcal{F}_d = 0.005$ (anomalous dispersion). This is an example of the quasi-continuous residual spectrum forming the quasi-smooth line converging to $g/\kappa = 1/2$, see the last column in Table I for scaling of g/κ to the intra-resonator cw power, g/γ . Yellow shading shows the range corresponding to the middle branch of the cw-state. Magenta line is the cw-state for $\mathcal{W}/\mathcal{W}_* = 2$. **(b)** Normalised threshold laser power, see Eq. (24), vs δ_0/κ computed using the $g_\mu^{(i)}$ data from (a) taken outside the yellow shading, so that the plot applies to the upper branch of the cw-resonance. The colorbar shows the number of the simultaneously growing sideband pairs. Magenta line is drawn at $\mathcal{W}/\mathcal{W}_* = 2$.

and for $D_2 < 0$ at $\delta_0 > 0$, i.e., along the lower branch, see Fig. 1.

The $g_0^{(2)} < g < g_0^{(1)}$ condition corresponding to the yellow shaded regions in Figs. 2(a), and 3(a),(c) is an important reference condition. If one tunes the input power, \mathcal{W} , then the tip of the nonlinear cw-resonance, i.e., the point where the upper and middle branches connect, slides along the $g = g_0^{(1)}$ line. Simultaneously, the turning point connecting the middle and lower branches slides along the $g = g_0^{(2)}$. Hence, the cw-solution can either go through the parameter ranges providing uninterrupted FWM gain, or cut across one or more isolated Arnold tongues, so that the instability and stability in-

tervals intermit, see and compare Figs. 2(a), 3(a),(c). As soon as the g/κ vs δ_0 cw tail drops below $1/2$, then the FWM instability becomes prohibited, as per Eqs. (22). Nonlinear transformation $g \rightarrow \mathcal{W}$, Eq. (12), maps the magenta coloured bistable cw-states in Figs. 2(a), 3(a) to the horizontal lines corresponding to the constant power levels in the (δ_0, \mathcal{W}) plots, Figs. 2(b), 3(b).

The yellow shading in Figs. 2(a), 3(a),(c) embraces all and only parameter values belonging to the middle branch of the bistability loop. δ_0 point where the middle and upper branches merge is slightly shifted from the $\max_{\delta_0}(g)$ point, see Fig. 5(b). The instability tongues that unfold to the right for $\mathcal{F}_d < 0$ in Fig. 3(c) belong to

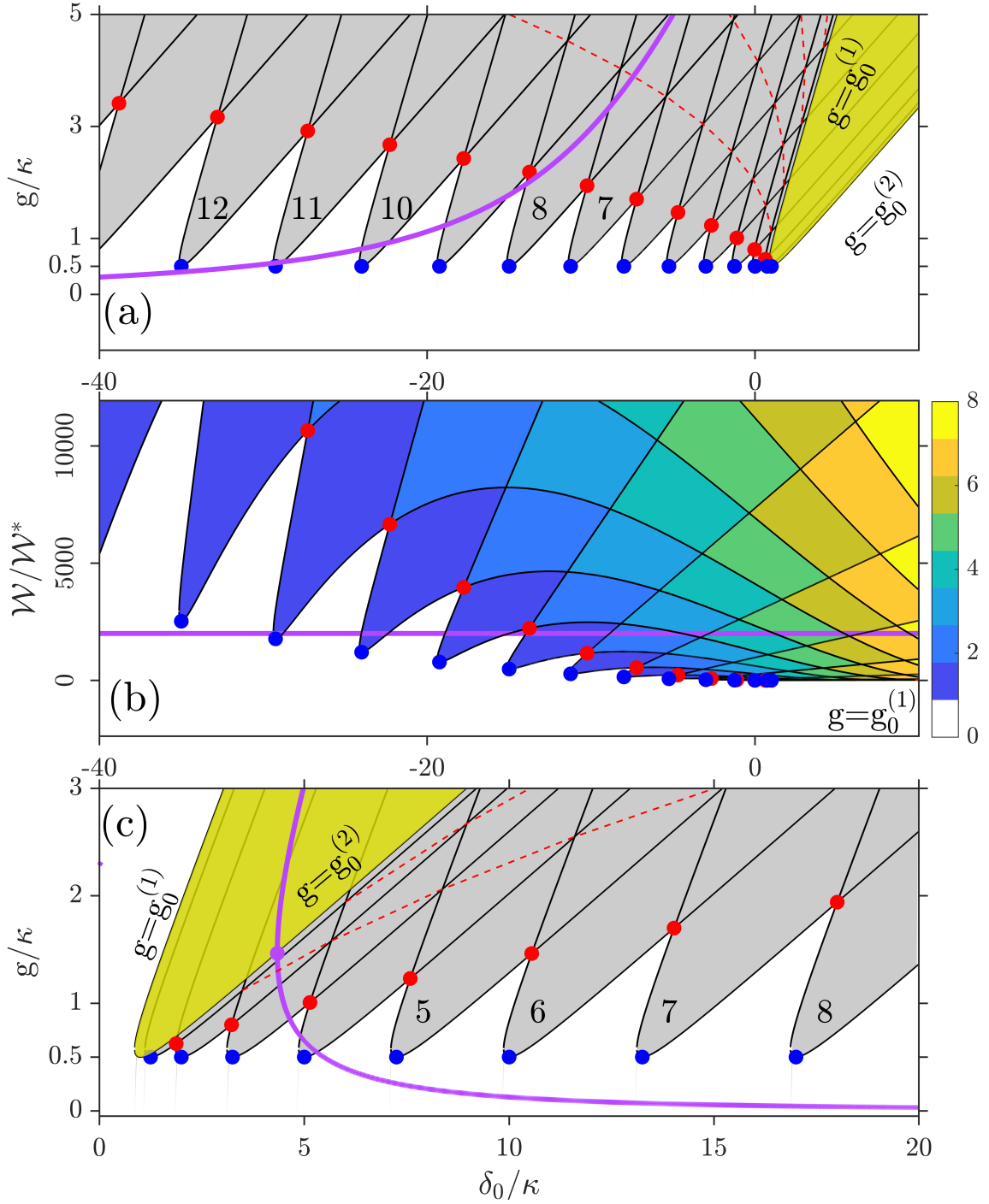


FIG. 3. An illustration of how the sparse residual spectrum, $|\mathcal{F}_d| = |D_2|/\kappa \sim 1$, leads to the very different FWM (blue points) and complexity (red points) thresholds. **(a)** $g = g_\mu^{(i)}$ vs δ_0 for $\mu = 0, 1, \dots, 13$ and $\mathcal{F}_d = 0.5$ (anomalous dispersion). Yellow shading shows the range of parameters corresponding to the middle branch of the cw-state, $g_0^{(2)} < g < g_0^{(1)}$. Grey shading shows the range of $\mu \neq 0$ instabilities. Magenta line shows the $\delta_0 < 0$ tail of the upper branch of the cw-state for $\mathcal{W}/\mathcal{W}_* = 2000$. The in-figure numbers show $|\mu|$ for the respective tongues. For the chosen $\mathcal{W}/\mathcal{W}_*$, the $|\mu| = 9, 10, 11$ tongues make isolated in δ_0 instability intervals. One sideband pair, $\pm\mu$, is unstable inside the quasi-rhombi starting at the blue points, i.e., FWM threshold. Two pairs, $\pm\mu, \pm(\mu+1)$, are simultaneously unstable inside the quasi-rhombi extending upwards from the red points, i.e., threshold of complexity. **(b)** Normalised threshold laser power, see Eq. (24), vs δ_0/κ computed using the $g_\mu^{(i)}$ data from (a) taken outside the yellow shading. The colorbar shows the number of the simultaneously growing sideband pairs. Magenta line is drawn at $\mathcal{W}/\mathcal{W}_* = 2000$. **(c)** is like (a), but for $\mathcal{F}_d = -0.5$ (normal dispersion). Magenta line shows the lower and middle branches of the cw-state, $\mathcal{W}/\mathcal{W}_* = 50$. The $|\mu| = 4$ tongue makes an isolated instability interval around $\delta_0/\kappa \approx 5$. For scaling of g/κ in (a) and (c) to the intra-resonator cw power g/γ , see the last column in Table I.

the lower branch of the cw-state in Fig. 1. Similarly, the tongues that unfold to the left for $\mathcal{F}_d > 0$ in Figs. 2(a), 3(a) belong to the upper branch.

Eqs. (16), (24) divide the (δ_0, g) and (δ_0, \mathcal{W}) parameter spaces into the well defined sections corresponding to the simultaneous growth of one, two, three and more pairs of modes, see Figs. 2(b), 3(b). In the $|\mathcal{F}_d| \ll 1$ case, see Fig. 2(b), these sections form a quasi-continuous pattern with the density of states increasing with g . The areas immediately above the threshold line for the negative and positive δ 's are however structured differently. For $\delta < 0$, the segments along the instability boundaries contain only one unstable $\pm\mu$ pairs, while for the different $|\mu|$ accumulate together for $\delta > 0$.

If $|\mathcal{F}_d|$ is brought close to 1, see Fig. 3(b), then the density of the quasi-rhombs becomes much lower. Simultaneously, the parameter space, across the range of the relatively small pump powers and for $\delta < \kappa$, becomes divided into $|\mu|$ -specific instability tongues separated by the stability intervals. Crossing into the first layer of rhombs in Fig. 3(b), i.e., into the rhombs having their bottom vertices marked with the blue points, implies instability of only one $\pm\mu$ sideband pair. Crossing into the second layer of rhombs having their bottom vertices marked with the red points implies the simultaneous instability relative to the $\pm\mu$ and $\pm(\mu \pm 1)$ sideband pairs, and so on.

The blue dots at the minima of the tongues correspond to the conditions in Eq. (22) and they make a threshold that is referred here as the FWM threshold. Reaching the FWM threshold implies exponential amplification of the sideband pairs, but the pump frequency needs to be tuned carefully to trigger frequency conversion into a particular $\pm\mu$ pair. When the second layer of rhombs is reached, see red dots, only then the stability gaps between the tongues disappear and the simultaneous instabilities of the $|\mu|$ and $|\mu \pm 1|$ sidebands become possible. Note, that the red dots are the cusps, and are not differentiable in δ_0 , unlike the blue dots found from the $\partial_{\delta_0} g_\mu^{(2)} = 0$ condition, Eq. (22). The line of the red dots is referred by us as the *threshold of complexity* [19]. This is the first and only in the sequence of the higher-order thresholds that touches the intervals of the cw-state stability. \mathcal{W}_* provides quite a small scale, see Table I. So that, fixing $\mathcal{W}/\mathcal{W}_* = 5000$, the two ultrahigh-Q cases, see Fig. 3, give $\mathcal{W} = 0.5\text{mW}$ (CaF₂) and 200mW (Si₃N₄) of the on-chip laser power, and only few Watts of the intra-resonator powers. So that, the tongue structure and complexity threshold are within a practical rich even in cases of smaller Q 's.

Section IV accomplishes formulating formal conditions for the first and the higher-order lines of the cusp points and solves these conditions for Δ_μ , δ_0 , g and power values along the threshold of complexity are derived in Section V.

Before moving on, let us remark, that the external contour of the power plot for $|\mathcal{F}_d| \ll 1$, see Fig. 2(b), should be compared with the same thresholds derived

and discussed in Ref. [16]. The equation for the contour in Fig. 2(b) is found by applying $g_\mu^{(i)}/\kappa = 1/2$ in Eq. (24),

$$\frac{\mathcal{W}}{\mathcal{W}_*} = \frac{1}{2} + 2 \left(\frac{\delta_0}{\kappa} - \frac{1}{2} \right)^2, \quad (25)$$

and should be used for $\delta_0 < \delta_0^{(0F)} = \kappa$, $\mathcal{F}_d > 0$. Substitution of $g = g_\mu^{(1)}$ in Eq. (24) follows the contour in Fig. 2(b) for $\delta_0 > \kappa$. Eq. (25) also applies for $\delta_0 > \delta_0^{(0F)}$, but if one takes the lower cw branch and $\mathcal{F}_d < 0$.

IV. THRESHOLD OF COMPLEXITY: DETUNINGS AT THE CUSPS

We now focus on the development of the analytical theory for the threshold of complexity. The $|\mu|$ specific instability boundaries consist in general from the two different conditions, $g = g_\mu^{(1)}$ and $g = g_\mu^{(2)}$. In order to look into how these two conditions interact along the threshold of complexity, we make two new g vs δ_0 plots, see Fig. 4, and assign the black color to the $g = g_\mu^{(1)}$ and the red one to $g = g_\mu^{(2)}$ conditions, respectively. We note, that

$$\Delta_\mu = \Delta_{-\mu}, \quad g_\mu^{(i)} = g_{-\mu}^{(i)}, \quad (26)$$

and hence fixing $\mu \geq 0$ does not restrict generality of the theory developed below.

A. Red-red intersections

For the relatively small $|\mathcal{F}_d|$, there exists a range of δ_0 where the complexity threshold is made by the intersections of the $g = g_\mu^{(2)}$ and $g = g_{\mu+1}^{(2)}$ lines, i.e., by the red-red intersections, see Fig. 4(a). The range of $|\mathcal{F}_d|$ providing the red-red intersections is limited from above $|\mathcal{F}_d| < |\tilde{\mathcal{F}}_d|$, where $\tilde{\mathcal{F}}_d$ is worked out later, see Eq. (43). For either sign of \mathcal{F}_d the coordinates of the red-red intersections are found by solving

$$g = g_\mu^{(2)} = g_{\mu+1}^{(2)}, \quad (27)$$

Applying Eqs. (16), (27) we find

$$|\mathcal{F}_d| < |\tilde{\mathcal{F}}_d|, \quad \frac{2\Delta_\mu}{\kappa} - \sqrt{\frac{\Delta_\mu^2}{\kappa^2} - \frac{3}{4}} = \frac{2\Delta_{\mu+1}}{\kappa} - \sqrt{\frac{\Delta_{\mu+1}^2}{\kappa^2} - \frac{3}{4}}. \quad (28)$$

Introducing the residual finesse, as given by Eq. (7a), to link $\Delta_{\mu+1}$ and Δ_μ gives

$$\begin{aligned} 0 &= 2\alpha_\mu + \sqrt{\frac{\Delta_\mu^2}{\kappa^2} - \frac{3}{4}} - \sqrt{\left(\frac{\Delta_\mu}{\kappa} + \alpha_\mu\right)^2 - \frac{3}{4}} \\ &= \mathcal{R}_{22}(\alpha_\mu, \Delta_\mu). \end{aligned} \quad (29)$$

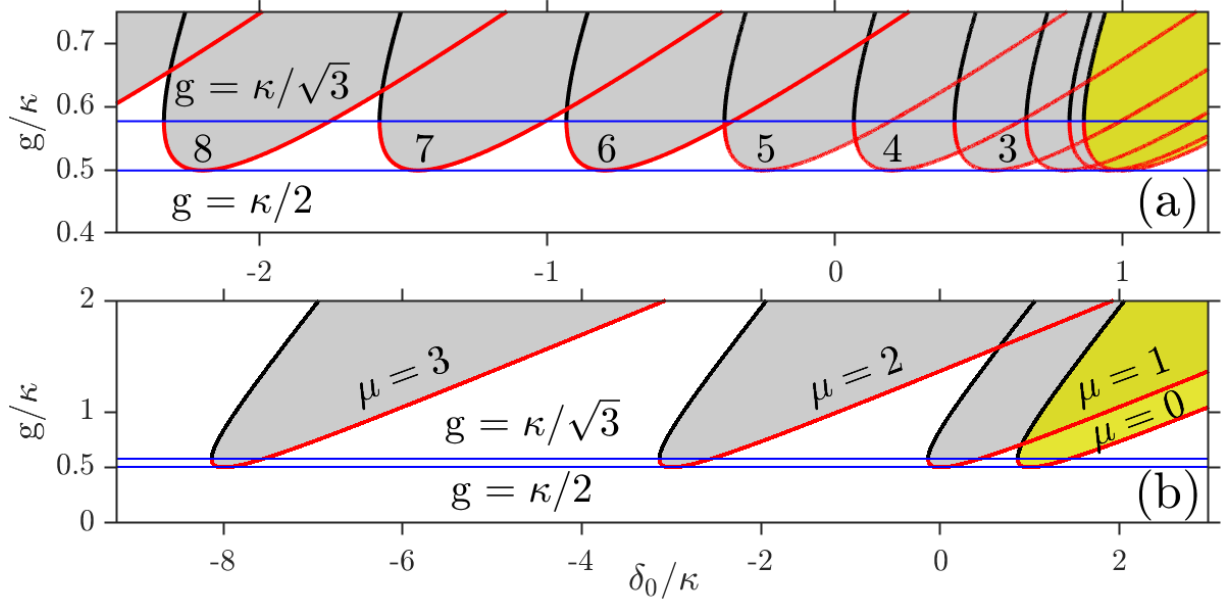


FIG. 4. (a) $\mathcal{F}_d = 0.1$: Transition from the red-red crossing of the μ and $\mu + 1$ instability lines to the red-black ones, $\hat{\mu} \approx 5.3$, $|\hat{\delta}_0/\kappa| \approx 0.4$, see section IV.C. The last red-red crossing is $\mu = 5$ to $\mu = 6$. (b) $\mathcal{F}_d = 1.5$: In this case, all the crossings are the red-black ones, since $\mathcal{F}_d > \tilde{\mathcal{F}}_d$. Blue lines show the minima of the tongues, i.e., FWM threshold, $g/\kappa = 1/2$, and the $g_\mu^{(1)} = g_\mu^{(2)}$ points, where $g/\kappa = 1/\sqrt{3}$, i.e., bistability threshold. Black and red lines correspond to $g_\mu^{(1)}$ and $g_\mu^{(2)}$, respectively.

Here, the subscript '22', reminds that Eq. (29) corresponds to the intersections between $g_\mu^{(2)}$ and $g_{\mu+1}^{(2)}$.

Squaring Eq. (29) twice yields an elegant equation for Δ_μ ,

$$\left(\frac{\Delta_\mu}{\kappa} + \frac{\alpha_\mu}{2}\right)^2 = 1 + \alpha_\mu^2. \quad (30)$$

Recalling Eq. (20) selects the positive root of Eq. (30), when it is solved for Δ_μ ,

$$\frac{\Delta_\mu}{\kappa} = \sqrt{1 + \alpha_\mu^2} - \frac{\alpha_\mu}{2}. \quad (31)$$

Inserting Eq. (31) back into Eq. (29) makes a function of a single variable α_μ , i.e., $\mathcal{R}_{22}(\alpha_\mu, \Delta_\mu(\alpha_\mu))$. \mathcal{R}_{22} is zero for

$$-|\alpha_{\hat{\mu}}| < \alpha_\mu < |\alpha_{\hat{\mu}}|, \quad (32)$$

where $\alpha_{\hat{\mu}}$ is a constant, see Fig. 5(a) and Eq. (39).

Recovering δ_0 from Eqs. (31), (4) yields

$$\frac{\delta_0^{(\mu C)}}{\kappa} = \sqrt{1 + \alpha_\mu^2} - \frac{\alpha_\mu}{2} - \frac{1}{2}\mu^2\mathcal{F}_d, \quad (33)$$

that holds at the red points in Figs. 1(b), 3(a), cf., Eq. (23) valid at the blue points.

Eq. (31) is derived again in the next subsection, where we point at its convergence to Eq. (22a) in the limit $\alpha_\mu \rightarrow 0$, and proceed with further important implications derived from this critical condition.

B. Red-black intersections

As $|\mu|$ is increased, the red-red crossings along the universal threshold are replaced with the red-black ones for $\mu > \hat{\mu}$, see Fig. 4(a). If $|\mathcal{F}_d|$ is large enough, i.e., $|\mathcal{F}_d| > |\tilde{\mathcal{F}}_d|$, then the intersections can become exclusively of the red-black type, including the $\mu = 0$ and $\mu = 1$ one, see Fig. 4(b). Both $\hat{\mu}$ and $\tilde{\mathcal{F}}_d$ are worked out below, see Eqs. (41), (43).

The red-black intersections for $\mathcal{F}_d > 0$ and $\mathcal{F}_d < 0$ are given by different conditions,

$$\mathcal{F}_d > 0: \quad g = g_\mu^{(1)} = g_{\mu+1}^{(2)}, \quad (34a)$$

$$\mathcal{F}_d < 0: \quad g = g_\mu^{(2)} = g_{\mu+1}^{(1)}. \quad (34b)$$

A reason for the two conditions here and one in the previous subsection is that now $g_\mu^{(1)}$ is matched with $g_{\mu+1}^{(2)}$, and in the previous case we matched $g_\mu^{(2)}$ with $g_{\mu+1}^{(2)}$, so that the ordering did not matter. An accompanying factor to account for is that the tongues tilt points in the direction of $|\mu|$ increasing for $\mathcal{F}_d > 0$, and towards $|\mu|$ decreasing for $\mathcal{F}_d < 0$, cf., Figs. 1(b) and 3(a).

Substituting Eqs. (16) to Eqs. (34) yields, respec-

tively,

$$\mathcal{F}_d > 0 : \frac{2\Delta_\mu}{\kappa} + \sqrt{\frac{\Delta_\mu^2}{\kappa^2} - \frac{3}{4}} = \frac{2\Delta_{\mu+1}}{\kappa} - \sqrt{\frac{\Delta_{\mu+1}^2}{\kappa^2} - \frac{3}{4}}, \quad (35a)$$

$$\mathcal{F}_d < 0 : \frac{2\Delta_\mu}{\kappa} - \sqrt{\frac{\Delta_\mu^2}{\kappa^2} - \frac{3}{4}} = \frac{2\Delta_{\mu+1}}{\kappa} + \sqrt{\frac{\Delta_{\mu+1}^2}{\kappa^2} - \frac{3}{4}}. \quad (35b)$$

Introducing α_μ , Eqs. (35) are replaced with

$$\begin{aligned} \mathcal{F}_d > 0 : 0 &= 2\alpha_\mu - \sqrt{\frac{\Delta_\mu^2}{\kappa^2} - \frac{3}{4}} - \sqrt{\left(\frac{\Delta_\mu}{\kappa} + \alpha_\mu\right)^2 - \frac{3}{4}} \\ &= \mathcal{R}_{12}(\alpha_\mu, \Delta_\mu), \end{aligned} \quad (36a)$$

$$\begin{aligned} \mathcal{F}_d < 0 : 0 &= 2\alpha_\mu + \sqrt{\frac{\Delta_\mu^2}{\kappa^2} - \frac{3}{4}} + \sqrt{\left(\frac{\Delta_\mu}{\kappa} + \alpha_\mu\right)^2 - \frac{3}{4}} \\ &= \mathcal{R}_{21}(\alpha_\mu, \Delta_\mu). \end{aligned} \quad (36b)$$

Resolving Eqs. (36) for Δ_μ also gives Eq. (31). Eq. (36a) and Eq. (36b) are satisfied for $\alpha_\mu > |\alpha_{\hat{\mu}}|$ and $\alpha_\mu < -|\alpha_{\hat{\mu}}|$, respectively, see Fig. 5(a).

Thus, Eq. (31) specifies Δ_μ , and hence δ_0 , at the cusp points along all of the threshold of complexity and should be compared with Eq. (22a) valid at the tongue minima along the FWM threshold.

In the limit $\alpha_\mu \rightarrow 0$, Eq. (31) transforms to Eq. (23) valid at the FWM threshold. Noting that $g_\mu^{(i)}$ are expressed via Δ_μ , we can claim that we have demonstrated analytically that the first line of cusps, i.e., the threshold of complexity, and the line of minima of $g_\mu^{(2)}$, i.e., the FWM threshold, converge to a single line in the limit of vanishing residual finesse, see Fig. 2.

The threshold where three pairs of side-bands become simultaneously unstable for $\mathcal{F}_d > 0$ is found from the condition $g_\mu^{(1)} = g_{\mu+2}^{(2)}$, and $\Delta_{\mu+1} - \Delta_\mu = \alpha_\mu$ in the above calculations should be replaced with $\Delta_{\mu+2} - \Delta_\mu = \alpha_\mu + \alpha_{\mu+1} = 2(\alpha_\mu + \frac{1}{2}\mathcal{F}_d)$. In general, a condition for $N \geq 2$ sidebands pairs, i.e., $\pm\mu, \pm(\mu+1), \dots, \pm(\mu+N-1)$, to become unstable is $g_\mu^{(1)} = g_{\mu+N-1}^{(2)}$. Δ_μ at the respective cusp points is found applying the substitution $\alpha_\mu \rightarrow \alpha_\mu^{(N)}$ in Eq. (31), where

$$\begin{aligned} \alpha_\mu^{(N)} &= (N-1) \left(\alpha_\mu + (N-2) \frac{\mathcal{F}_d}{2} \right), \\ N &= 2, 3, \dots; \quad \alpha_\mu = \alpha_\mu^{(2)}. \end{aligned} \quad (37)$$

Again, this applies for both the red-red and red-black intersections. Thin dashed red lines in Figs. (3)(a),(c) connect the cusp point along the $N = 3$, $N = 4$, and $N = 5$ thresholds. We note, that the explicit dependence on \mathcal{F}_d in Eq. (37) is weak, providing $\mu \gg \frac{1}{2}N$. Hence, using $\alpha_\mu^{(N)} \approx (N-1)\alpha_\mu$ is a good practical approximation for the cusp points along the higher order thresholds.

C. Crossover from the red-red to the red-black intersections: Critical mode number and critical detuning

In general, the red-red crossing make less contrasted tongues than the red-black ones. This is because the values of g/κ at the red-red points have to be below $g/\kappa = 1/\sqrt{3}$, see Eq. (21), so that they are closer to the minima of the tongues at $g/\kappa = 1/2$. While, the red-black intersections can rise arbitrarily far above the minima. Using this, we develop a more rigid criterion for transition from the quasi-continuous to the sparse residual spectrum, which is $|\alpha_\mu| < |\alpha_{\hat{\mu}}|$ for quasi-continuum, and $|\alpha_\mu| > |\alpha_{\hat{\mu}}|$ for the sparse residual spectrum. This approach also provides practical value for \mathcal{F}_d , $\mathcal{F}_d = \hat{\mathcal{F}}_d$, signalling that the spectrum is sparse starting from $\mu = 0$.

Eqs. (29) and (36) are resolved by Eq. (31) over different intervals of α_μ , due to different signs in front of the square roots in the $\mathcal{R}_{22} = 0$, $\mathcal{R}_{21} = 0$, and $\mathcal{R}_{12} = 0$ equations. Critical values of α_μ , where the just mentioned intervals touch, i.e., the red-red intersections change to the red-black ones, are found imposing

$$\mathcal{F}_d > 0 : \mathcal{R}_{22}(\alpha_\mu, \Delta_\mu) = \mathcal{R}_{12}(\alpha_\mu, \Delta_\mu) \Rightarrow \frac{\Delta_\mu^2}{\kappa^2} = \frac{3}{4}; \quad (38a)$$

$$\begin{aligned} \mathcal{F}_d < 0 : \mathcal{R}_{22}(\alpha_\mu, \Delta_\mu) &= \mathcal{R}_{21}(\alpha_\mu, \Delta_\mu) \\ &\Rightarrow \left(\frac{\Delta_\mu}{\kappa} + \alpha_\mu \right)^2 = \frac{3}{4}. \end{aligned} \quad (38b)$$

Combining Eq. (31) and Eq. (38a) gives

$$\mathcal{F}_d > 0 : \sqrt{1 + \alpha_{\hat{\mu}}^2} - \frac{1}{2}\alpha_{\hat{\mu}} = \frac{\sqrt{3}}{2} \Rightarrow \alpha_{\hat{\mu}} = \frac{1}{\sqrt{3}}. \quad (39)$$

Similarly, Eq. (31) and Eq. (38b) lead to

$$\mathcal{F}_d < 0 : \sqrt{1 + \alpha_{\hat{\mu}}^2} + \frac{1}{2}\alpha_{\hat{\mu}} = \frac{\sqrt{3}}{2} \Rightarrow \alpha_{\hat{\mu}} = \frac{-1}{\sqrt{3}}. \quad (40)$$

Recalling α_μ definition in Eq. (5a), we find that

$$\mu > \hat{\mu}, \text{ where } \hat{\mu} = \frac{1}{\sqrt{3}|\mathcal{F}_d|} - \frac{1}{2}, \quad \hat{\mu} \in \mathbb{R}, \quad (41)$$

corresponds to $|\alpha_\mu| > 1/\sqrt{3}$. This is quite a remarkable result that provides a resonator specific mode number signalling transition to the Arnold tongue regime with the threshold power sharply varying with the pump frequency.

Knowing $\hat{\mu}$, we can estimate the pump detuning, $\hat{\delta}_0$, required to cross into the Arnold regime. Using Eq. (22a) gives

$$\begin{aligned} \frac{|\delta_0|}{\kappa} &\gtrsim \frac{|\hat{\delta}_0|}{\kappa} = \left| 1 - \frac{1}{2}\hat{\mu}^2 \mathcal{F}_d \right| \\ &= \left| \frac{1}{6\mathcal{F}_d} - \left(1 + \frac{1}{2\sqrt{3}} - \frac{\mathcal{F}_d}{8} \right) \right|. \end{aligned} \quad (42)$$

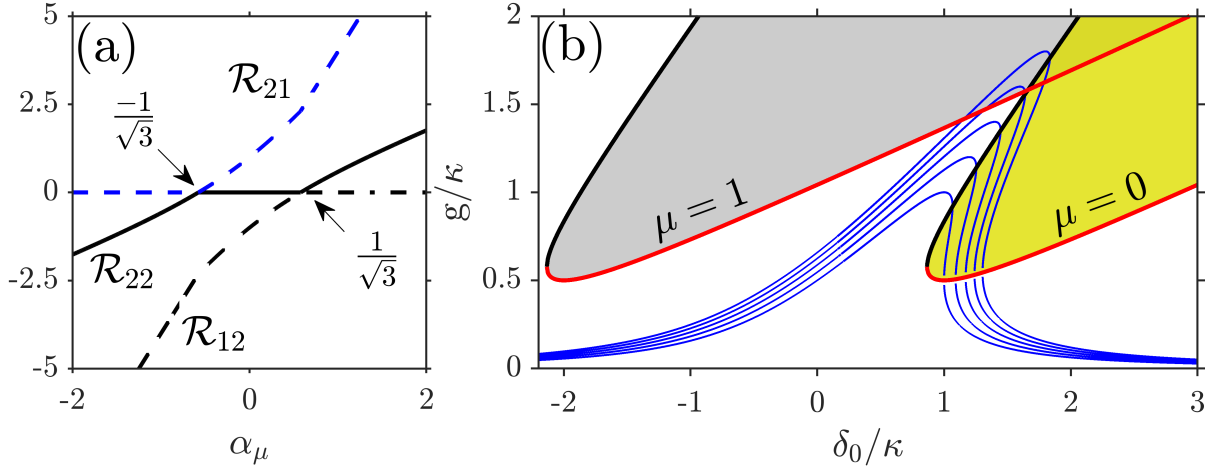


FIG. 5. (a) Functions $\mathcal{R}_{jj'}$ vs residual finesse, α_μ . $\mathcal{R}_{jj'} = 0$ constitute equations for the threshold of complexity. \mathcal{R}_{22} correspond to the red-red intersections, and \mathcal{R}_{12} , \mathcal{R}_{21} to the red-black ones, see Fig. 4. (b) Bistability without FWM for $F_d = 6$. First three blue lines show the bistable cw-states, when both the upper and lower branches are stable relative to the sideband excitations. Two top blue lines have the upper branch entering the $|\mu| = 1$ instability range. The pump values are $\mathcal{W}/\mathcal{W}_* = 1, 1.2, 1.4, 1.6, 1.8$ for the blue lines from bottom to top.

The above condition can be used to check if the Arnold regime is within a reach of the pump laser tuning range in cases when a resonator sample has $|\mathcal{F}_d| \ll 1$. This consideration has suggested the grouping of the terms in the last part of Eq. (42).

D. Bistability without FWM

$\mathcal{F}_d = \tilde{\mathcal{F}}_d$ marking the disappearance of the red-red crossings even from the $\mu = 0$ and $\mu = 1$ intersection for $|\mathcal{F}_d| > |\tilde{\mathcal{F}}_d|$, see Fig. 4(b), is found by taking $\hat{\mu} = 0$,

$$|\tilde{\mathcal{F}}_d| = \frac{|D_2|}{\kappa} = \frac{2}{\sqrt{3}} \approx 1.155. \quad (43)$$

Thus, from the point of view of Arnold tongues becoming a dominant feature of the FWM threshold, the whole of the residual spectrum starting from $\mu = 0$ can be considered as sparse providing $|\mathcal{F}_d| > |\tilde{\mathcal{F}}_d|$. Large spectral sparsity implies that the phase sensitive FWM terms that couple the $\mu = 0$ and $\mu = 1$ modes oscillate on the time scales that are fast enough for these terms to become negligible, so that the FWM instability become impossible.

It means that the point of the intersection between the $\mu = 0$ and $\mu = 1$ instabilities moves above the bistability point, $g_0^{(1)} = g_0^{(2)}$, in the (δ_0, g) -plane, see Fig. 5(b). Hence it opens up a range of pump powers and detunings that are sufficient to make the resonator bistable, i.e., $g/\kappa > 1/\sqrt{3}$, but still not high enough to trigger frequency conversion. This situation is not possible if the residual spectrum is continuous, making the frequency conversion to start at $g = \kappa/2$ and as soon as $\delta_0 < \delta_0^{(OF)} = \kappa$ (minimum point of $g = g_0^{(2)}$).

V. THRESHOLD OF COMPLEXITY: SIDEBAND COUPLING AND PUMP POWER

A. Sideband coupling

Results from the previous Section should now be used to calculate the coupling constant g along the threshold of complexity. This is accomplished by substituting Δ_μ from Eq. (31) into $g_\mu^{(i)}$ in Eq. (27) and Eqs. (34):

$$g = g_{\mu C}^{(2)}(\Delta_\mu(\alpha_\mu)) \quad \text{if } \alpha_\mu \in \left(-\infty, \frac{1}{\sqrt{3}}\right]; \quad (44a)$$

$$g = g_{\mu C}^{(1)}(\Delta_\mu(\alpha_\mu)) \quad \text{if } \alpha_\mu \in \left[\frac{1}{\sqrt{3}}, +\infty\right). \quad (44b)$$

The subscripts 'C' and 'F' indicate that the respective quantities are taken along either the threshold of Complexity or along the FWM one. Eqs. (23) and (33) used the same superscripts.

Fig. 6 shows plots of $g_\mu^{(i)}(\Delta_\mu(\alpha_\mu))$ vs α_μ , see Eq. (33). It also shows the horizontal line corresponding to the minima of the tongues, see Eqs. (22), i.e., to

$$g = g_{\mu F}^{(2)}(\Delta_\mu = \kappa) = \frac{\kappa}{2}. \quad (45)$$

Fig. 6 applies only to those ranges of the detunings where the FWM (blue dots) and complexity (red dots) thresholds exist, see Fig. 3.

The small and large $|\alpha_\mu|$ cases in Fig. 6 can be analysed by means of the asymptotic expansions, leading to the explicit expressions for $\mathcal{W}_{\mu C}$ and $\mathcal{W}_{\mu F}$. Eq. (31) and

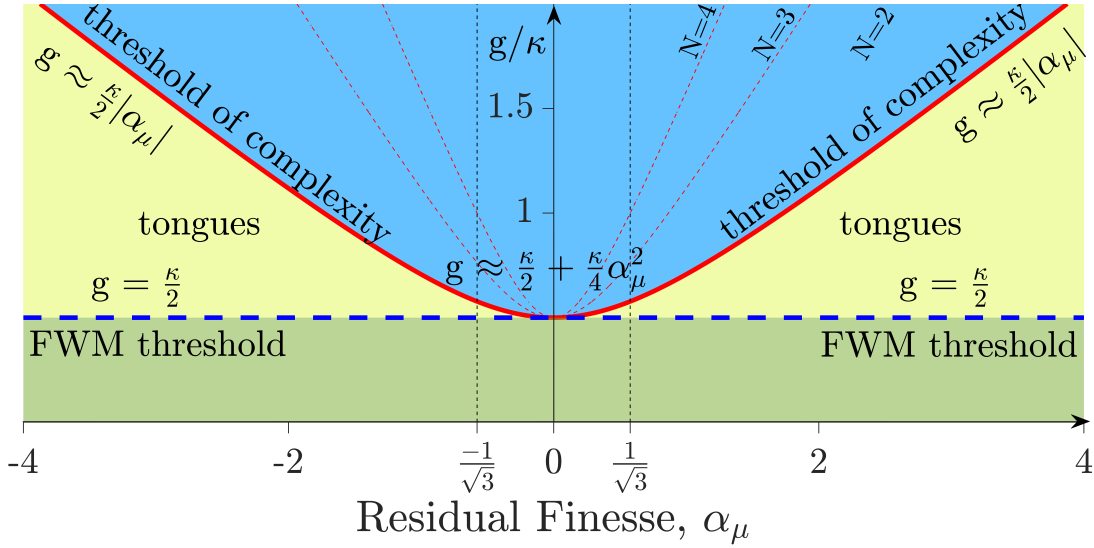


FIG. 6. FWM (blue dashed line) and complexity (red full line) thresholds in the sideband coupling strength, g , and the residual finesse, $\alpha_\mu \approx \mu \mathcal{F}_d$, parameter space. For scaling of g/κ to the intra-resonator cw power g/γ , see the last column in Table I. Green shading corresponds to the stable cw-state. Yellow shading corresponds to the $|\mu|$ -specific instability tongues, i.e., Arnold tongues, intermitting with the intervals of stability. Blue shading corresponds to the simultaneous instabilities with different $|\mu|$, and with the cw stability being fully lost. Dashed red lines show the higher-order thresholds for 3 and 4 sideband pairs to be unstable simultaneously.

Eqs. (16) in the respective limits become:

$$|\alpha_\mu| \gg \alpha_{\hat{\mu}}, \quad \frac{\Delta_\mu}{\kappa} = |\alpha_\mu| - \frac{\alpha_\mu}{2} + \mathcal{O}(\alpha_\mu^{-1}); \quad (46a)$$

$$\alpha_\mu \gg \alpha_{\hat{\mu}}, \quad \frac{g_{\mu C}^{(1)}}{\kappa} = \frac{\Delta_\mu}{\kappa} + \mathcal{O}(\frac{\kappa}{\Delta_\mu}) = \frac{1}{2}\alpha_\mu + \mathcal{O}(\alpha_\mu^{-1}); \quad (46b)$$

$$-\alpha_\mu \gg \alpha_{\hat{\mu}}, \quad \frac{g_{\mu C}^{(2)}}{\kappa} = \frac{\Delta_\mu}{3\kappa} + \mathcal{O}(\frac{\kappa}{\Delta_\mu}) = -\frac{1}{2}\alpha_\mu + \mathcal{O}(\alpha_\mu^{-1}). \quad (46c)$$

and

$$|\alpha_\mu| \ll \alpha_{\hat{\mu}}, \quad \frac{\Delta_\mu}{\kappa} = 1 - \frac{\alpha_\mu}{2} + \frac{\alpha_\mu^2}{2} + \mathcal{O}(\alpha_\mu^4); \quad (47a)$$

$$\frac{g_{\mu C}^{(2)}}{\kappa} = \frac{1}{2} + \frac{\alpha_\mu^2}{4} + \mathcal{O}(\alpha_\mu^4). \quad (47b)$$

In the limit $\alpha_\mu \rightarrow 0$, $g_{\mu C}^{(2)}$ in Eq. (47b) naturally tends to $g_{\mu F}^{(2)}$ in Eq. (45). The same calculations can be repeated with $\alpha_\mu^{(N)}$, Eq. (37), to find thresholds corresponding to the simultaneous instabilities of the N pairs of sidebands. If the approximation discussed after Eq. (37) is applied, then the respective $g_{\mu C}^{(i)}$ are still solely parametrised by α_μ , which is used in Fig. 6 to plot $N = 3$, and $N = 4$ thresholds.

Fig. 6 is, in essence, a summary of our results. It shows that the values of the sideband coupling constant, g , and the residual finesse, α_μ , specify three possible regimes of the resonator operation along the tails of

the cw-resonance in Fig. 1: (i) green area: stable cw-state; (ii) red area: $|\mu|$ -specific instability tongues, i.e., Arnold tongues, intermitting with the intervals of stability; (iii) blue area: simultaneous instabilities of the tongues with different $|\mu|$, and with the cw stability being fully lost.

B. Pump power

Practical approximations for the laser power along the threshold of complexity can also be worked out using that the tongues are largely located along the tails of the cw-state, where $|\delta_0|/g \gg 1$, see Fig. 3, and hence, Eq. (12) is reduced to

$$\frac{\mathcal{W}}{\mathcal{W}_*} \approx \frac{g}{\kappa} \frac{4\delta_0^2}{\kappa^2}. \quad (48)$$

Minima of the laser power are then $\partial_{\delta_0}[\mathcal{W}/\mathcal{W}_*] \approx 4\delta_0^2[\partial_{\delta_0}g](1 + \mathcal{O}(g/\delta_0))/\kappa^3$, and are closely matched by the minima of $g_{\mu C}^{(2)}$, see Eqs. (22).

For $|\mu| \gg 1$, which is also consistent with $|\delta_0|/g \gg 1$,

$$\delta_0^{(\mu C)} \approx \delta_0^{(\mu F)} \approx -\frac{1}{2}\mu^2 D_2, \quad (49)$$

see Eqs. (23), (33). Using Eqs. (45) we then find

$$\frac{\mathcal{W}_{\mu F}}{\mathcal{W}_*} \approx \frac{2\delta_0^2}{\kappa^2} \approx \frac{\mathcal{F}_d^2 \mu^4}{2} \quad (50)$$

for the FWM threshold, and, using Eqs. (46),

$$\frac{\mathcal{W}_{\mu C}}{\mathcal{W}_*} \approx \frac{2\delta_0^2}{\kappa^2} \frac{\sqrt{2}|\delta_0 D_2|}{\kappa} \approx \frac{|\mathcal{F}_d|^3 |\mu|^5}{2} \quad (51)$$

for the threshold of complexity.

Thus, $|\alpha_\mu| \approx |\mu\mathcal{F}_d|$ is the factor making the difference between the FWM and complexity thresholds in the large detuning limit,

$$\frac{\mathcal{W}_{\mu C}}{\mathcal{W}_{\mu F}} \approx |\alpha_\mu|, \quad \frac{|\delta_0|}{g} \gg 1. \quad (52)$$

The above ratio also measures the relative contrast of the Arnold tongues.

Let us recall, that $\mathcal{W}_* \sim \kappa^2$, see Eq. (10). Thus in the dispersive limit, $|\delta_0| \gg g$, the FWM threshold power for large $|\mu|$ scales with D_2^2 , and is κ independent in the leading order. The complexity-threshold power scales inversely with κ and is also more sensitive to D_2 . The $\mathcal{W}_{\mu C} \sim 1/\kappa$ scaling may look counter-intuitive at first glance, but is in fact natural, since the complexity means the simultaneous instability of different $|\mu|$, which is harder to achieve if the linewidth is narrow, i.e., $|\mathcal{F}_d| = |D_2|/\kappa$ is large. In the small $|\delta_0|/\kappa$ limit, the threshold power scales with κ^2 as is given by \mathcal{W}_* , see Eq. (25).

VI. TOPICAL CONNECTIONS AND FURTHER DIRECTIONS

The threshold of complexity also has its counterpart in the theory of nonlinear lattices in the condensed matter and optical contexts. Namely, this is the Peierls-Nabarro (PN) potential barrier, which constitutes the energy difference between the localised nonlinear lattice excitations centred on one lattice site and the two neighbouring sites [36, 37]. The latter requires higher energy. Here, we have dealt with the frequency-space version of the PN-barrier. Indeed, the threshold of complexity is the two-mode-number, $\pm\mu, \pm(\mu+1)$, excitation threshold requiring higher energy than the one-mode-number, $\pm\mu$, threshold.

Ref. [19] has made a particular emphasis on the synchronisation physics, that has allowed to associate the instability domains in our system with the classic Arnold tongues and to make several cross-disciplinary links [29]. While, our work is focused on the parameter range outside the soliton regime, the Arnold-tongue connected soliton physics achieved via synchronisation of the fibre-coupled pair of resonators [34] and via the soliton-breather period synchronising to the repetition rate [35] has also attracted recent attention.

Arnold tongues in a proximity of the zero dispersion and in the presence of the higher-order dispersion terms, e.g., in connections to recent experimental results in Ref. [38], and in the few photon regimes [39, 40] emerge as the interesting problems to look at. Boundaries of the tongues are the bifurcation lines, where new solutions are emerging. These solutions are the Turing roll patterns. While Refs. [25, 30–32], see also references therein and thereafter, cover the prior work on Turing rolls in Kerr resonators with continuous or quasi-continuous residual

spectra, our Ref. [19] has found that inside the Arnold tongues these structures demonstrate frequency domain symmetry breaking, and transition to the multimode chaos on approach to the threshold of complexity. Further understanding of these and search for new properties of the Turing rolls in the high- \mathcal{F}_d case call for a dedicated near future investigation.

VII. SUMMARY

We have presented a comprehensive theory of the interplay between the finesse dispersion, $\mathcal{F}_d = D_2/\kappa$, and the frequency conversion thresholds in the Kerr microresonators when the pump frequency is scanned along the dispersive tails of the nonlinear resonance. The linear stability analysis of the dispersive tails of the cw-state predicts sharp variations in the threshold power in the resonators with the ultrahigh finesse, $\mathcal{F} = D_1/\kappa$, and large \mathcal{F}_d . Large areas of the cw-stability separated by the instability tongues and located above the minimal intra-resonator powers required for FWM come as a surprise, see Figs. 3, 6.

Our theory reveals the key role played by the residual finesse parameter, $\alpha_\mu \approx \mu\mathcal{F}_d$, in determining the difference between the power thresholds for the simultaneous excitation of the two pairs of modes, $\pm\mu, \pm(\mu+1)$, (threshold of complexity) and for one pair, $\pm\mu$ (FWM threshold). We have determined the critical value of \mathcal{F}_d , i.e., $|\mathcal{F}_d| \geq 2/\sqrt{3}$, for the FWM-free bistability and the pronounced tongue structure to start at the near-zero detunings. If $|\mathcal{F}_d| < 2/\sqrt{3}$, then the tongues become pronounced for the detunings exceeding the critical value, $|\delta_0|/\kappa > 1/6|\mathcal{F}_d| + \dots$.

Overall, our work underpins development of the microresonator based frequency conversion sources by predicting optimal pump laser frequencies and powers for achieving mode-number specific conversion in the high-finesse devices.

ACKNOWLEDGEMENT

We acknowledge discussions with Z. Fan.

FUNDING

EU Horizon 2020 Framework Programme (812818, MICROCOMB).

APPENDIX: PARAMETER ESTIMATES

Estimates for the crystalline, e.g., CaF_2 [5, 22], resonators are $S = 100\mu\text{m}^2$, $n_0 = 1.43$, $n_2 = 1.71 \times 10^{-20}\text{m}^2/\text{W}$, $\omega_0 = 200\text{THz}$, and hence $\gamma \simeq 10\text{kHz}/\text{W}$. 2mm radius corresponds to $D_1/2\pi = 16\text{GHz}$.

D_2 can be either positive or negative and order of few kHz, we take $D_2 = 1\text{kHz}$. The linewidth $\kappa/2\pi = 200\text{kHz}$ corresponds to the quality factor $Q = 10^9$ and finesse $\mathcal{F} \simeq 10^5$. So that $W_* = \pi\kappa^2/\eta D_1\gamma \simeq 1\text{mW}$, $\eta = 0.5$, $|\mathcal{F}_d| = 0.005$. Taking an ultrahigh-Q resonator with $\kappa/2\pi = 2\text{kHz}$, $Q = 10^{11}$ gives $\mathcal{W}_* \simeq 0.1\mu\text{W}$, and $|\mathcal{F}_d| = 0.5$.

Estimates for the integrated Si_3N_4 resonators [3, 4, 11, 17] are $S = 0.5\mu\text{m}^2$, $n_0 = 2$, $n_2 = 2.4 \times 10^{-19}\text{m}^2/\text{W}$,

$\omega_0 = 200\text{THz}$, and hence $\gamma \simeq 20\text{MHz}/\text{W}$. $23\mu\text{m}$ radius corresponds to $D_1/2\pi = 1\text{THz}$. D_2 can be either positive or negative, we take $D_2 = 50\text{MHz}$ for the width $\simeq 1.5\mu\text{m}$ and height $\simeq 0.8\mu\text{m}$. The linewidth $\kappa/2\pi = 100\text{MHz}$ corresponds to the quality factor $Q = 2 \times 10^6$ and finesse $\mathcal{F} \simeq 10^4$. So that $W_* \simeq \pi\kappa^2/\eta D_1\gamma \simeq 4\text{mW}$, $\eta = 0.5$, $|\mathcal{F}_d| = 0.5$. Taking an ultrahigh-Q resonator with $\kappa/2\pi = 10\text{MHz}$, $Q = 2 \times 10^7$ gives $\mathcal{W}_* \simeq 40\mu\text{W}$, and $|\mathcal{F}_d| = 5$. Concise summary of the scaling powers is given in Section II.C, Table I.

-
- [1] H. Kimble, The quantum internet, *Nature* **453**, 1023 (2008).
 - [2] S.A. Diddams, K. Vahala, and T. Udem, Optical frequency combs: Coherently uniting the electromagnetic spectrum, *Science* **369**, eaay3676 (2020).
 - [3] Z. Ye, K. Twayana, P. A. Andrekson, and V. Torres-Company, High-Q Si_3N_4 microresonators based on a subtractive processing for Kerr nonlinear optics, *Opt. Express* **27**, 35719-35727 (2019).
 - [4] H. El Dirani, L. Youssef, C. Petit-Etienne, S. Kerdiles, P. Grosse, C. Monat, E. Pargon, and C. Sciancalepore, Ultralow-loss tightly confining Si_3N_4 waveguides and high-Q microresonators, *Opt. Express* **27**, 30726-30740 (2019).
 - [5] A. A. Savchenkov, A. B. Matsko, V.S. Ilchenko, and L. Maleki, Optical resonators with ten million finesse, *Opt. Express* **15**, 6768-6773 (2007).
 - [6] L. Wu, H. Wang, Q. Yang, Q. Ji, B. Shen, C. Bao, M. Gao, and K. Vahala, Greater than one billion Q factor for on-chip microresonators, *Opt. Lett.* **45**, 5129-5131 (2020).
 - [7] L. Chang, W. Xie, H. Shu, Q. Yang, B. Shen, A. Boes, J.D. Peters, W. Jin, C. Xiang, S. Liu, G. Moille, S. Yu, X. Wang, K. Srinivasan, S.B. Papp, K. Vahala, and J.E. Bowers, Ultra-efficient frequency comb generation in AlGaAs-on-insulator microresonators, *Nat. Commun.* **11**, 1331 (2020).
 - [8] W.E. Lamb, Jr., Theory of an Optical Maser, *Phys. Rev.* **134**, A1429 (1964).
 - [9] H. Risken and K. Nummedal, Self-Pulsing in Lasers, *J. Appl. Phys.* **39**, 4662 (1968).
 - [10] L. A. Lugiato and F. Castelli, Quantum noise reduction in a spatial dissipative structure, *Phys. Rev. Lett.* **68**, 3284 (1992).
 - [11] T.J. Kippenberg, A.L. Gaeta, M. Lipson, and M.L. Gorodetsky, Dissipative Kerr solitons in optical microresonators, *Science* **361**, eaan8083 (2018).
 - [12] Y.K. Chembo and C.R. Menyuk, Spatiotemporal Lugiato-Lefever formalism for Kerr-comb generation in whispering-gallery-mode resonators, *Phys. Rev. A* **87**, 053852 (2013).
 - [13] T. Herr, V. Brasch, J.D. Jost, C.Y. Wang, N.M. Kondratiev, M.L. Gorodetsky, and T.J. Kippenberg, Temporal solitons in optical microresonators, *Nat. Phot.* **8**, 145-152 (2014).
 - [14] T. Hansson, D. Modotto, and S. Wabnitz, On the numerical simulation of Kerr frequency combs using coupled mode equations, *Opt. Commun.* **312**, 134 (2014).
 - [15] C. Milián and D.V. Skryabin, Soliton families and resonant radiation in a micro-ring resonator near zero group-velocity dispersion, *Opt. Express* **22**, 3732-3739 (2014).
 - [16] C. Godey, I.V. Balakireva, A. Coillet, and Y.K. Chembo, Stability analysis of the spatiotemporal Lugiato-Lefever model for Kerr optical frequency combs in the anomalous and normal dispersion regimes, *Phys. Rev. A* **89**, 063814 (2014).
 - [17] L.A. Lugiato, F. Prati, M.L. Gorodetsky and T.J. Kippenberg, From the Lugiato-Lefever equation to microresonator-based soliton Kerr frequency combs, *Phil. Trans. R. Soc. A* **376**, 20180113 (2018).
 - [18] D.V. Skryabin, Hierarchy of coupled mode and envelope models for bi-directional microresonators with Kerr nonlinearity, *OSA Continuum* **3**, 1364-1375 (2020).
 - [19] D.V. Skryabin, Z. Fan, A. Villosio, and D.N. Puzyrev, Threshold of complexity and Arnold tongues in Kerr ring microresonators, *Phys. Rev. A* **103** (Letters), (2021), [in press](#).
 - [20] Y.K. Chembo, and N. Yu, Modal expansion approach to optical-frequency-comb generation with monolithic whispering-gallery-mode resonators, *Phys. Rev. A* **82**, 033801 (2010).
 - [21] T.J. Kippenberg, S.M. Spillane, and K.J. Vahala, Kerr-Nonlinearity Optical Parametric Oscillation in an Ultrahigh-Q Toroid Microcavity, *Phys. Rev. Lett.* **93**, 083904 (2004).
 - [22] A.A. Savchenkov, A.B. Matsko, D. Strekalov, M. Mohageg, V.S. Ilchenko, and L. Maleki, Low Threshold Optical Oscillations in a Whispering Gallery Mode CaF_2 Resonator, *Phys. Rev. Lett.* **93**, 243905 (2004).
 - [23] P. Del'Haye, A. Schliesser, O. Arcizet, T. Wilken, R. Holzwarth, and T. J. Kippenberg, Optical frequency comb generation from a monolithic microresonator, *Nature* **450**, 1214-1217 (2007).
 - [24] A.B. Matsko, A.A. Savchenkov, D. Strekalov, V.S. Ilchenko, and L. Maleki, Optical hyperparametric oscillations in a whispering-gallery-mode resonator: Threshold and phase diffusion, *Phys. Rev. A* **71**, 033804 (2005).
 - [25] L.A. Lugiato and R. Lefever, Spatial Dissipative Structures in Passive Optical Systems, *Phys. Rev. Lett.* **58**, 2209 (1987).
 - [26] P. Lodahl, A.F. van Driel, I.S. Nikolaev, I.A. Irman, K. Overgaag, D. Vanmaekelbergh, and W.L. Vos, Controlling the dynamics of spontaneous emission from quantum dots by photonic crystals, *Nature* **430**, 654-657 (2004).
 - [27] D. Englund, D. Fattal, E. Waks, G. Solomon, B. Zhang, T. Nakaoka, Y. Arakawa, Y. Yamamoto, and J. Vuckovic, Controlling the spontaneous emission rate of single quantum dots in a two-dimensional photonic crystal,

- Phys. Rev. Lett. **95**, 013904 (2005).
- [28] C. Kittel, *Introduction to Solid State Physics* (Wiley, 1996).
 - [29] A. Pikovsky, M. Rosenblum, and J. Kurths, *Synchronization: A universal concept in nonlinear sciences* (Cambridge University Press, 2001).
 - [30] A.J. Scroggie, W.J. Firth, G.S. McDonald, M. Tlidi, R. Lefever, and L.A. Lugiato, Pattern formation in a passive Kerr cavity, *Chaos Solitons & Fractals* **4**, 1323-1354 (1994).
 - [31] P. Parra-Rivas, D. Gomila, L. Gelens, and E. Knobloch, Bifurcation structure of periodic patterns in the Lugiato-Lefever equation with anomalous dispersion, *Phys. Rev. E* **98**, 042212 (2018).
 - [32] Z. Qi, S. Wang, J. Jaramillo-Villegas, M.H. Qi, A.M. Weiner, G. D'Aguanno, T.F. Carruthers, and C.R. Menyuk, Dissipative cnoidal waves (Turing rolls) and the soliton limit in microring resonators, *Optica* **6**, 1220-1232 (2019).
 - [33] D. Romanini, I. Ventrillard, G. Méjean, J. Morville, and E. Kerstel, Introduction to Cavity Enhanced Absorption Spectroscopy; in *Cavity Enhanced Spectroscopy and Sensing*, G. Gagliardi and H.-P. Loock, eds. (Springer, 2013).
 - [34] J.K. Jang, X. Ji, C. Joshi, Y. Okawachi, M. Lipson, and A.L. Gaeta, Observation of Arnold Tongues in Coupled Soliton Kerr Frequency Combs, *Phys. Rev. Lett.* **123**, 153901 (2019).
 - [35] D.C. Cole and S.B. Papp, Subharmonic Entrainment of Kerr Breather Solitons, *Phys. Rev. Lett.* **123**, 173904 (2019).
 - [36] Y.S. Kivshar and D.K. Campbell, Peierls-Nabarro potential barrier for highly localized nonlinear modes, *Phys. Rev. E* **48**, 3077 (1993).
 - [37] R. Morandotti, U. Peschel, J. S. Aitchison, H. S. Eisenberg, and Y. Silberberg, Dynamics of Discrete Solitons in Optical Waveguide Arrays, *Phys. Rev. Lett.* **83**, 2726 (1999).
 - [38] N. Sayson, T. Bi, V. Ng, H. Pham, L.S. Trainor, H.G.L. Schwefel, S. Coen, M. Erkintalo, and S.G. Murdoch, Octave-spanning tunable parametric oscillation in crystalline Kerr microresonators, *Nat. Photon.* **13**, 701-706 (2019).
 - [39] P.B. Main, P.J. Mosley, and A.V. Gorbach, Parametric resonances and resonant delocalisation in quasi-phase matched photon-pair generation and quantum frequency conversion, *New J. Phys.* **21**, 093023 (2019).
 - [40] D. Roberts and A.A. Clerk, Driven-Dissipative Quantum Kerr Resonators: New Exact Solutions, Photon Blockade and Quantum Bistability, *Phys. Rev. X* **10**, 021022 (2020).